Comparison of ionospheric anomalies over African equatorial/low-latitude region with IRI-2016 model predictions during the maximum phase of solar cycle 24

Paul O Amaechi, Elijah O Oyeyemi, Andrew O Akala, Mohamed Kaab, Waqar Younas, Zouhair Benkhaldoun, Majid Khan, Christine-Amory Mazaudier

Comparison of Ionospheric Anomalies over African Equatorial/Low-latitude Region with IRI-2016 Model Predictions during the Maximum Phase of Solar Cycle 24

[*]Paul O. Amaechi[1], Elijah O. Oyeyemi[2], Andrew O. Akala[2,3], Mohamed Kaab[4,5], Waqar Younas[6], Zouhair Benkhaldoun[4], Majid Khan[6], Christine-Amory Mazaudier[7,8]

[1]Department of Physical Sciences, Chrisland University, Abeokuta, Nigeria
[2]Department of Physics, University of Lagos, Akoka, Yaba, Lagos, Nigeria
[3]Maritime Institute, University of Lagos, Akoka, Yaba, Lagos, Nigeria
[4]Oukaimeden Observatory, LPHEA, FSSM, Cadi Ayyad University, Marrakech, Morrocco
[5]National School of Applied Sciences of Beni Mellal, Sultan Moulay Sliman University, Beni Mellal, Morocco
[6]Department of Physics, Quaid-i-Azam University, Islamabad 45320, Pakistan
[7]LPP, CNRS/Ecole Polytechnique/Sorbonne Université/Université Paris-Sud/Observatoire de Paris, 75006 Paris, France
[8] T/ICT4D Abdus Salam ICTP, Italy

*Corresponding author: Paul O. Amaechi (email: paoloobiaks@yahoo.fr)
Tel: +2348032050324

Abstract

The capability of IRI-2016 in reproducing the hemispheric asymmetry, the winter and semiannual anomalies has been assessed over the equatorial ionization anomaly (EIA) during quiet periods of years 2013-2014. The EIA reconstructed using Total Electron Content (TEC) derived from Global Navigation Satellite System was compared with that computed using IRI-2016 along longitude 25^o - 40^{o}E. These were analyzed along with hemispheric changes in the neutral wind derived from the horizontal wind model and the TIMED GUVI columnar O/N_2 data. IRI-2016 clearly captured the hemispheric asymmetry of the anomaly during all seasons albeit with some discrepancies in the magnitude and location of the crests. The winter anomaly in TEC which corresponded with greater O/N_2 in the winter hemisphere was also predicted by IRI-2016 during December solstice. The model also captured the semiannual anomaly with stronger crests in the northern hemisphere. Furthermore, IRI-2016 reproduced the variation trend of the asymmetry index (A) in December solstice and equinox during noon. However, in June solstice the model failed to capture the winter anomaly and misrepresented the variation of A. This was linked with its inability to accurately predict the pattern of the neutral wind, the maximum height of the F2 layer and the changes in O/N_2 in both hemispheres. The difference between variations of EUV and F10.7 fluxes was also a potential source of errors in IRI-2016. The results highlight the significance of the inclusion of wind data in IRI-2016 in order to enhance its performance over East Africa.

Keywords: IRI-2016, Equatorial Ionization Anomaly, Hemispheric asymmetry, Winter anomaly, Semiannual anomaly.

1. Introduction

The ionosphere is the ionized part of the atmosphere which extends from about 60 to 1000 km (Hargreaves, 1995) and comprises of free ions and electrons in sufficient number as to affecting radio signals. Ionospheric anomalies which were first reported in the works of earlier scientists (Appleton, 1938; Berkner et al., 1936) have been the subject of various investigations over the years. Ionospheric anomaly originally referred to departures from the solar controlled behavior in which the critical frequency foF2 varies regularly with the solar zenith angle (χ) as it does in the well-known Chapman layer (Rishbeth, 1998). According to Rishbeth (1998) the term anomaly originally meant ‘‘any departure from solar controlled behavior in which the critical frequency foF2 varies regularly with the solar zenith angle (χ) as it does in the well-known Chapman layer’’.

Salient ionospheric anomalies are the seasonal anomaly otherwise known as the winter anomaly, the annual anomaly or non-seasonal anomaly and the semiannual anomaly as well as the equatorial ionization anomaly (EIA).

The winter anomaly is characterized by greater peak electron density of the F2 layer (NmF2) in the winter hemisphere than its conjugate summer hemisphere during solstices (Torr and Torr, 1973). For the annual anomaly, the NmF2 is significantly greater in December than June solstice globally (Gowtam and Tulasi Ram, 2017) while for the semiannual anomaly it is higher in equinox than solstice (Rishbeth, 1998; Yasyukevich et al., 2018). The EIA also known as the Appleton Anomaly (Appleton, 1946), is an essentially feature of the low-latitude ionosphere. It is discernable by the reduction in ionization at the magnetic equator (the trough) as against two peaks on both sides of it at about $\pm 15^{o}$ magnetic latitude (the crests) (Namba and Maeda, 1939).

Several mechanisms have been put forth to explain the ionospheric anomalies. It has been suggested that the winter anomaly is caused by change in neutral composition, driven by global thermospheric circulation, which is greater in winter than in summer (Burns et al., 2014; Rishbeth and Setty, 1961; Zou et al., 2000). The annual anomaly is driven by the higher December solstice solar flux which is responsible for greater dissociation of molecular oxygen than June solstice (Yonezawa and Arima, 1959) as well as by changes in the Sun-Earth distance, difference between the geographic and magnetic equator and the tilt of the geomagnetic dipole (Zeng et al., 2008). The semiannual anomaly is easily explained in terms of stronger (weaker) vertical drifts and ionization due to the fact that photoionization is more effective in equinox (solstice) (Fejer et al., 1995) as well as greater O/N_2 ratio in equinox as compared to solstice (Rishbeth et al., 2000; Zhao et al., 2007). The EIA is brought about by the fountain effect (Mitra, 1946) which is the upward transport of plasma by an **E**x**B** force above the magnetic equator, and it subsequent diffusion along the magnetic field lines under the effects of gravity and pressure gradient (Karia et al., 2018; Sterling et al., 1969).

The EIA is however, far from being symmetric (Oyedokun et al., 2020). This is because of the presence of transequatorial neutral winds which affect the equatorial plasma diffusion resulting in significant asymmetry through the transport of plasma from one

hemisphere to the other (e.g., Heelis and Hanson 1980; Khadka et al., 2018). This in conjunction with the highest Total Electron Content (TEC) values at the EIA crests are sources of additional errors in critical navigation and positioning applications. The delay suffered by a radio wave propagating through the ionosphere is proportional to TEC and could be significantly high at the EIA crests. This in turn will translate to increase positioning errors, especially in single-frequency Global position System (GPS) receivers. More so, the increased in ionospheric electrodynamical and chemical processes at the EIA will undoubtedly affect the performance of models, especially over least studied region such as Africa. This poses serious concern to the modeling community and underscores the significance of our study.

The International Reference Ionosphere (IRI) is an empirical model aimed at establishing an international standard for specifying the climatology of ionospheric parameters (Bilitza and Reinisch, 2008). It is widely accepted as a standard model to describe ionospheric features in various applications such as communication, aviation, navigation. IRI is constantly being ameliorated using a wide range of ground and space data, Global Navigation Satellite System (GNSS) networks, ionosondes and satellite data. This has led to the existence of several versions of the model of which IRI-2016 is the latest (Bilitza et al., 2017).

IRI has been extensively utilized in various longitudinal sectors to study the dynamics of the ionosphere. However, studies carried out over Africa have shown that even the latest version of IRI (IRI-2016) is susceptible to prediction errors (Endeshaw, 2020; Melaku and Tsidu, 2019; Mengistu et al., 2019; Mengistu and Melaku, 2020). Unfortunately, due to the limited number of simultaneous studies in both hemispheres, there is little information on the performance of IRI-2016 over the African EIA. Particularly, there are no studies assessing the capability of the model to reproduce the interhemispheric asymmetry as well as the winter and semiannual anomalies. In addition, the global success of IRI and its application in critical GNSS systems require that its level of accuracy over all regions of the globe be ascertained. This is more pertinent over the Africa longitude which has long been poorly represented in the existing global database (Bilitza et al., 2014).

The aim of this work is to investigate ionospheric anomalies over the African equatorial/low-latitude region and then examine how IRI-2016 reproduces the observed hemispheric asymmetry in the EIA, winter and semiannual anomalies during the maximum phase of solar cycle 24 (SC-24). This falls well within the scope of the Committee on Space Research / International Union of Radio Science (COSPAR /URSI) IRI Working Group session (at the 43rd COSPAR Scientific Assembly), which is geared towards improving the description of hemispheric differences in IRI.

2. Data and method of analysis

2.1 Data sets

In this study archived daily GNSS observation data in the Receiver Independent Exchange (RINEX) format with 30 seconds resolution have been utilized. The corresponding TEC data predicted by the recent version of the IRI-2016 model was also employed. The geographic location of the GNSS stations is shown in Fig. 1. We have also exploited the O/N_2 ratio data obtained from the Global Ultraviolet Imager (GUVI) on board the Thermosphere, Ionosphere, Mesosphere, Energetics and Dynamics (TIMED) satellite. Furthermore, the direction and magnitude of the meridional winds were derived from the recent version of the Horizontal Wind Model (HWM14) (Drob et al., 2015). Finally, the daily Extreme Ultraviolet (EUV) flux (26–34 nm) and solar flux (F10.7) measurements as well as the planetary K-index *(Kp)* were utilized. A summary of the sources of data and links to access them is given in Table 1.

All these data sets were obtained during quiet days of years 2013 and 2014. Both years fall within the maximum phase of SC-24 with mean observed annual solar flux of 122.76 and 146.54 solar flux unit (s.f.u), respectively. A day was deemed quiet if its *Kp* was lesser or equal to 3 (Amaechi et al., 2020; Fejer et al., 2008).

2.2 Method of analysis

2.2.1 TEC derived from GNSS measurements (GNSS-TEC)

For the estimation of GNSS-TEC, we first subjected the GNSS observables to quality check using the Translating Editing and Quality Checking (TEQC) software

(Estey and Meertens, 1999). Then, we analyzed them following the procedure of Seemala and Delay (2010). This entailed estimating slant TEC (STEC) which is also known as relative TEC using the so called carrier phase to code leveling technique described in Hansen et al. (2000). The algorithm of Blewitt (Blewitt, 1990) was used to detect and correct eventual cycle slips in phase measurements.

The STEC obtained was thereafter, calibrated by removing satellite and receiver biases (Sardon et al., 1994). This calibrated STEC was then converted to vertical TEC (VTEC) using the thin shell ionospheric model described by Mannucci et al. (1993). The effect of multipath was minimized by using an elevation cut-off mask of 30^o. The EIA was reconstructed using hourly averages of VTEC values at ionospheric pierce point (IPP) using GNSS station within 25^o - 40^oE with a latitudinal extent of ± 30^o geographic latitude. The temporal and spatial resolution of the EIA maps obtained was 1 hour x 1 degree. We recall that there is a displacement of about 9^o between the magnetic equator and geographic equator within longitude 25^o - 40^oE (Amaechi et al., 2020).

2.2.2 TEC derived from IRI model (IRI-TEC)

Hourly values of the TEC were derived from IRI-2016 with the NeQuick option for the topside electron density profile (Ne) and the latest bottomside thickness option (ABT-2009) selected. In addition, the Consultative Committee International Radio (CCIR) for F-peak option was used since it is the recommended option for the continent (Tariku, 2020). Also, the F-peak storm model option was set to off because we are considering geomagnetically quiet days. Finally, the required modeled TEC were obtained by integrating the Ne profile from an altitude of 90 - 2000 km (upper boundary for IRI model). The IRI-TEC so derived was utilized to reconstruct the EIA using the same spatio-temporal resolution with GNSS-TEC. Because of the difference in the upper boundary of integration between IRI (2000 km) and GNSS (20,200 km), we excluded the contribution of the plasmaspheric electron contribution (PEC) to GNSS-TEC data. Details about the estimation technique can be found in Akala et al. (2015), Cherniak et al. (2012) and Karia et al. (2015; 2018).

The interhemispheric asymmetry was quantified using the asymmetry index (A) computed with both GNSS-TEC and IRI-TEC data. A is a good measure of the

asymmetry of the anomaly (Paul and DasGupta, 2010). It was computed in the local noon (1200 – 1700 LT) and post sunset (1900 – 2200 LT) using equation 1. Both time intervals correspond to periods when the anomaly is fully developed in Africa (Amaechi et al., 2018).

$$A = \frac{A_1 - A_2}{S} \quad \text{Eq. (1)}$$

where A_1 and A_2 are the areas computed under the TEC- latitude plot on both sides of the magnetic equator up to the crest in both hemispheres and S is the strength of the anomaly defined by $S = \frac{A_1 + A_2}{2}$ and A is the asymmetry index.

In the computation of A1 and A2, we first calculated the areas of small polygons whose vertices were defined by the TEC and the corresponding magnetic latitude. Then, we integrated the estimated areas of the polygons to get total area under the curve. Positive (negative) value of A is an indication of stronger winter crest in in December (June) solstice.

2.2.3 Thermospheric composition (O/N_2) ratio and meridional winds (U)

To take into account thermospheric composition changes, we computed the O/N_2 ratio during quiet days of year 2013 and 2014 for longitude 25^o - 40^oE. This data set is available in IDLsave format at guvitimed.jhuapl.edu and comprises of O/N_2 measurements as function of latitude, longitude and UT time as the spectrometer takes the measurements at a specific location. We have averaged daily measurements corresponding to the Northern hemisphere (0:30^{o}N) and Southern hemisphere (0:30^{o}S), separately along longitude 25^o - 40^oE. Thereafter seasonal averages of O/N_2 were calculated by taking arithmetic mean of all available data points belonging to respective geographic location.

The meridional wind velocity was calculated using the technique described in Amaechi et al. (2020). The estimation technique which takes into account the recommendation of Chartier et al. (2015) is described in details in Kaab et al. (2017). It entails estimating the airglow-weighted meridional winds, U, between 200 and 300 km using equation 2.

$$U = \frac{\sum u_z a_z}{a_z} \quad \text{Eq. (2)}$$

where u_z and a_z are the meridional winds from HWM14 and the calculated redline volume emission rate at altitude z, respectively (Link and Cogger, 1988).

The seasonal profiles of wind over longitude 25^o - 45^{o}E with a latitudinal extent of ±30^o were reconstructed using data from all the stations in Fig. 1. This was done by averaging the wind data binned over 1 hours and 1 degree.

The seasonal variations of all parameters of interest (TEC, O/N_2, U, EUV and F10.7 fluxes) were examined. We took monthly average of November, December and January (May, June and July) to represent December (June) solstice and the average of February, March and April (August, September and October) for March (September) equinox.

3. Results

3.1 The winter anomaly

In Fig. 2 the seasonal variations of the EIA reconstructed using GNSS-TEC and IRI-TEC are shown during solstices of years 2013 and 2014. In this figure, the summer and winter hemispheres are respectively indicated for June/December solstice. It could be seen that the anomaly reconstructed using GNSS-TEC showed a conspicuous hemispheric asymmetry with stronger crest in the winter than summer hemisphere in December solstice. This was reproduced by IRI-2016 with the model showing higher crests magnitude with farther location in December solstice 2013. In 2014 nevertheless, the predicted crests magnitude were lower than the observed one while the crests location remained farther. In June solstices the observed and predicted anomalies were both asymmetric. However, the anomaly reconstructed using GNSS (IRI) measurements showed a stronger crest in the winter (summer) hemisphere. In addition, the predicted crests magnitude was conspicuously higher than the observed one.

The variations of the asymmetry index (A) during noon and post sunset are shown in Fig. 3(a-b). In the noon of both solstices, IRI-2016 underestimated the magnitude of A (Fig. 3a). The underestimation was nevertheless pronounced in June solstice. The model

further rightly (wrongly) predicted the sign of the asymmetry in December (June) solstice. The same trend of prediction of the sign of A was observed in the post sunset (Fig. 3b). However, the model underestimated the magnitude of A in June solstice while there was no significant difference in the observed and predicted magnitude and sign of A in December solstice. Fig. 3(c-d) depicts a typical example of variation of the peak height of the F2 layer (hmF2) obtained from IRI-2016 during solstices. In reconstructing this figure, we took the average of the hmF2 in both hemispheres during the local noon (1200 – 1700 LT) and post sunset (1900 – 2200 LT). Generally, it could be seen that hmF2 was higher in the northern than southern hemisphere. Furthermore, it was higher in December solstice than June solstice. The values obtained in the northern (southern) hemisphere during noon were 379 (326 km) and 401 (391 km) for June and December solstice, respectively (Fig. 3c). For the post sunset, they were 369 (327 km) and 452 (421 km) (Fig. 3d).

3.2 The semiannual anomaly

Fig. 4 presents the variations of GNSS-TEC and IRI-TEC in equinox and solstices in the years 2013 and 2014. The black solid lines indicate the location of the magnetic equator. We have combined TEC data for both equinoxes in order to clearly observe the semiannual anomaly. In addition to the hemispheric asymmetry observed during solstices, the equinoctial crests had different amplitudes with the stronger crests and larger latitudinal extent in the northern hemisphere. IRI-2016 clearly reproduced this asymmetry but showed relatively stronger (weaker) crests magnitude in the northern (southern) hemisphere than GNSS especially, in 2013. In 2014 nevertheless, IRI-2016 predicted weaker magnitude of the crests in both hemispheres. During all seasons, the model also clearly reproduced the solar activity dependence of TEC over the EIA with stronger (weaker) crests magnitude in 2014 (2013). The respective observed annual solar flux was 122.72 (146.54 sfu).

Fig. 5 shows the variations of A during equinox and solstices of years 2013 and 2014. It could be seen that the smallest magnitude of A computed using GNSS-TEC was observed in equinox during noon (Fig. 5a) and post sunset (Fig. 5b). Contrastingly, the model showed that the smallest magnitude of A occurred in June solstice during noon.

During post sunset however, it rightly predicted its occurrence in equinox. Also, the model rightly (wrongly) captured the sign of A and overestimated (underestimated) its magnitude during noon (post sunset). We finally noted a significant reduction in the observed and predicted magnitudes of A during equinox. We recall that the model predicted the asymmetry of the EIA but failed to capture its direction in June solstice (Fig. 5a-b). This was related to IRI's inability to correctly represent variations of hmF2 in both hemispheres during June solstice (Fig. 3c-d) as shown earlier. This also underpinned the inability of IRI-2016 to represent the direction of interhemispheric winds as pointed earlier.

3.3 Change in thermospheric composition

The seasonal variations in O/N_2 ratio in both hemispheres from 2013 to 2014 are shown in Fig. 6. From this figure, O/N_2 was higher in the southern/winter hemisphere than northern /summer hemisphere in June solstice. In December solstice, the reverse was the case with O/N_2 being higher in the northern/winter than southern/summer hemisphere. Also, O/N_2 was the highest in both hemispheres in equinox than solstices. It was equally found that March equinox had the higher O/N_2 ratio than September equinox. However, the difference in the equinoctial O/N_2 ratio between both hemispheres was not significantly different.

3.4 Thermospheric neutral wind

The seasonal variations of thermospheric neutral wind velocity in the years 2013 and 2014 are shown in Fig. 7. The broken horizontal lines represent the magnetic equator. Positive (negative) value of the velocity indicates a northward (southward) wind while the level of the contour on the color bar gives the wind's magnitude. From this figure December solstice was essentially marked by northward wind with higher velocities in the northern than southern hemisphere. A southward wind was however observed from 05:00 – 09:00 UT within latitude 10^oS to 30^oS (Fig. 7a). In the post sunset to post midnight period, the northward wind reached its highest velocity of about 120 m/s away from both crests. In the early morning of June solstice, the neutral wind was mostly northward with a velocity lesser than 20 m/s. From 05:00 – 09:00 UT, it was predominantly northward (southward) in the northern (southern) hemisphere with a

higher velocity in the southern hemisphere. It turned southward from 10:00 – 20:00 UT with a velocity higher than 40 m/s in the southern hemisphere. During equinoxes, the wind velocity was generally lesser than 60 m/s. In March equinox, from 0500 – 1100 UT, the wind was northward (southward) in the northern (southern) hemisphere. It later turned northward (southward) within 15^{o}S - 30^{o}N (15^{o}S – 30^{o}S) from 12:00 – 17:00 UT. Thereafter, it was directed northward within 8^{o}S to 30^{o}N and 10^{o}S – 30^{o}S. In September equinox, it was mostly northward in the northern hemisphere while from 5^{o}S - 30^{o}S, it turned southward within 04:00 – 16:30 UT. From 17:00 – 24:00 UT, the wind was northward with a velocity that decreased from southern hemisphere towards the equator and increased towards the northern hemisphere thereafter. From Fig. 7b, the seasonal pattern of neutral wind in 2014 was similar to that in 2013 (Fig. 7a) except for the fact that its velocity was relatively smaller in 2014 than 2013.

Fig. 8 presents the seasonal correlation between EUV (26 – 34 nm) and F10.7 solar fluxes in the years 2013 and 2014. We computed the coefficient of determination (R^2) which indicates the proportion of the variation in the dependent variable (F10.7 flux data) explained by the independent variables (EUV flux data) in the linear regression model. The MATLAB code used for the calculation of R^2 is based on comparing the variability of the estimation errors with that of the original values. From the computed values of R^2, it could be seen that there was a good agreement between EUV and F10.7 with about 84 – 90% of the earlier data set being related linearly to the earlier in December solstice 2013 and June solstice 2014. On the other hand, there was a slight reduction in the relation between both quantities in March equinox 2013 to December solstice 2014. During these seasons, it was found that about 62 – 74% of EUV flux data was still related to solar flux data. Nevertheless, in March and September equinox 2014, there was a weak relation between both solar parameters with only 27 – 39% of data being linearly related.

4. Discussion

In this section, we have discussed the mechanisms that modulated the hemispheric asymmetry of the EIA, winter and semiannual anomalies. These included the meridional wind, change in thermospheric composition and the fountain effect. Thereafter, the capability of IRI-2016 in reproducing these anomalies was assessed while plausible

reasons for the model's eventual misrepresentation of observed hemispheric features were proffered.

4.1 The winter and semiannual anomalies

It was observed that over longitude 25 - 40^{o}E, the transequatorial neutral winds blew from the summer to the winter hemisphere during solstices (Fig. 7) while the EIA was stronger in the winter than summer hemisphere (Fig. 2). Ordinarily, summer-to-winter winds drag ionization along the field lines, uplifting (lowering) the F-layer in the summer (winter) hemisphere (Balan et al. 1995; Kwak et al., 2019; Titheridge 1995). However, the summer-to-winter winds affect the fountain effect by reducing (enhancing) the diffusion of plasma into the EIA in the summer (winter) hemisphere (Gowtam and Tulasi Ram, 2017; Tulasi Ram et al. 2009). As such, the pattern of winds which drove the observed asymmetry of the anomaly (Fig. 3a-b) was favorable to plasma diffusion in the winter hemisphere and contributed to the enhancement of ionization over the crest in that hemisphere.

On the other hand, the O/N_2 ratio which was found to be higher in the winter than summer hemisphere (Fig. 6) also played a crucial role in driving the winter anomaly over Africa. The larger (smaller) O/N_2 in the winter (summer) hemisphere results from the summer-to-winter difference in solar radiation and the consequent the global thermospheric circulation (Burns et al., 2014; Qian et al., 2016; Qian and Yue, 2017; Yasyukevich et al., 2018). The changes in O/N_2 ratio in turn lead to the changes in the production/loss rate of electrons with greater changes in the winter hemisphere resulting in higher ionization (Millward et al., 1996). The greater density ratio of O/N_2 in winter than in summer was thus, responsible for the winter anomaly as pointed out by Rishbeth (1998).

The observed semiannual anomaly with higher TEC over the crests of the anomaly in both hemispheres during equinox (Fig. 4) followed the seasonal pattern of the change in thermospheric composition (higher O/N_2 in equinox than solstices) (Fig. 6). In addition, the semiannual anomaly was dominant in the northern hemisphere. This was in line with the higher O/N_2 observed in that hemisphere. This feature was also obvious in parameter A which showed that the anomaly was deflected northward in the noon during

equinox (Fig. 5). These results are in line with those of Rishbeth et al. (2000) who found that the O/N_2 ratio was greater in equinox than solstice at low-latitude. Zhao et al. (2007) had suggested that the O/N_2 variation contributes to some good extent to the semiannual annual anomaly of TEC possibly because of the dynamics associated with thermospheric neutral wind and electric fields at low-latitude. Results of the seasonal variation of the asymmetry index (A) revealed that the EIA was less asymmetric in equinox than solstice. This was consistent with the reduction in the neutral wind velocity in equinox (Fig. 7) and re-emphasized the role of neutral wind in driving seasonal variation over the EIA.

The semiannual anomaly of TEC at the EIA could also be explained in terms of solar EUV and change in electrodynamics. It is well known that the intensity of solar radiation which depends on the Sun's elevation is responsible for ionization in the ionosphere. During equinox, the Sun is overhead at the equator and more ionization is produced. Also, the vertical plasma drift velocity (Vz) which results from the interaction of the eastward electric field and horizontal magnetic field play a significant role in the transport and redistribution of plasma at low-latitude. Vz is stronger in equinox than solstice over the African longitude (Amaechi et al., 2018; Fejer et al., 1995). The implication is that the fountain effect will be stronger in equinox and more plasma will be lifted up and diffused towards the crests. Consequently, the anomaly will appear stronger and well-developed in equinox than solstice.

4.2 IRI prediction of the winter and semiannual anomalies

IRI-2016 reproduced the hemispheric asymmetry as well as the winter anomaly in December solstice (Fig. 2). The model also predicted the direction of the asymmetry as it rightly showed a stronger anomaly in the northern (winter) hemisphere. However, the model underestimated the magnitude of the asymmetry index especially during noon (Fig. 3a-b). This underestimation could have been due to the model's inability to capture the magnitude of the neutral wind in December solstice. In June solstices, IRI-2016 still reproduced the hemispheric asymmetry but failed to capture the winter anomaly. The model further misrepresented the direction of the asymmetry (showing a stronger anomaly in the summer instead of the winter hemisphere) and underestimated its magnitude. To have an insight into the model's misrepresentation of the winter anomaly

and the asymmetry of the anomaly in June solstice, we examined the hmF2 values obtained from IRI-2016 for both hemispheres in June and December solstices (Fig. 3c-d). It was found that the model did not show higher hmF2 in the southern (winter) hemisphere in June solstice. We thus, inferred that the misrepresentation of hmF2 in both hemispheres during June solstice could be a reason for the model's failure to capture the winter anomaly. Given the difference in the pattern of wind during both solstices (Fig. 7), we further deduce that IRI-2016 could not capture the direction of the interhemispheric wind and by extension the change in thermospheric composition in both hemispheres. This finding therefore calls for the inclusion of neutral wind data from the African longitude into IRI-2016 in order to ameliorate its predictive capability. Our result is in line with Kumar (2020) who reported greater departure of IRI-2016 from observed in-situ measurements of CHAMP and GRACE during June solstice over longitude 79^{o}E. In the same vein, Karia et al. (2018) showed that IRI-2016 had more discrepancies in the southern hemisphere of the EIA over longitude 73^{o}E in June solstice of 2012.

It was also found that IRI-2016 correctly predicted the semiannual anomaly and rightly showed that equinox had the stronger crests in both hemispheres (Fig. 4). Furthermore, the model captured the stronger crests in the northern hemisphere along with the reduction in the magnitude of the asymmetry especially in the post sunset. It further represented the solar activity dependence of TEC over the EIA with stronger and well-developed crests in 2014 (which had a higher solar flux than 2013). IRI-2016 nevertheless, overestimated the magnitude of the asymmetry during noon and misrepresented its direction in the post sunset of equinox. It equally overestimation /underestimated the magnitude of the northern/southern crest in 2013 while it underestimated it in 2014. The discrepancies in the model's predictive capability of the semiannual anomaly could be related to its inability to accurately represent the variations in electric field and consequently the fountain effect. Any misrepresentation of the equatorial electrojet (EEJ) which is a proxy of Vz will translate to differences between the observed and modeled TEC at the EIA. For example, Silva et al. (2020) showed that over the Brazilian region, the vertical drift could be responsible for deviations in the spatio-temporal features of the EIA crests in 2014/2015. In the same vein, Sousasantos et al. (2020) established that the Scherliess and Fejer model (Scherliess and Fejer, 1999)

which drives Vz in IRI had intrinsic trend of underestimation that appears to be independent of latitude and season. Recently, Mengistu et al. (2018) and Kumar (2020) advocated the inclusion of the EEJ measurements in the IRI model in order to increase its predictive capability over the African and Indian low-latitude, respectively. We however, note that given the extreme variability of the EEJ (Doumouya and Cohen, 2004; Venkatesh et al., 2015), long term measurements will be needed in Africa in order to clearly understand its variability before inclusion in IRI. Unfortunately, instruments such as incoherent scatter radar (ISR) which are capable of providing direct measurements of EEJ are quite scanty over the African longitude.

In addition, the difference between the variability of F10.7 and EUV fluxes could also be a major source of discrepancies in IRI-2016. F10.7 flux which is often taken as an input in the IRI model is just a proxy of EUV flux. EUV flux is the main solar flux parameter which exerts a greater control on ionization in the ionosphere (Kumar, 2016). If the variability of EUV is not well-reproduced by F10.7, then the output IRI parameter (e.g., IRI-TEC in our case) will not matched the observed one (GNSS-TEC). The analysis of the relation between EUV and F10.7 fluxes in 2013 and 2014 revealed that the nature of this relation varies significantly from one season to another (Fig. 8). This clearly implies that F10.7 flux does not always follows the trend of EUV flux. Emmert et al. (2010) had stressed on the difference between EUV and F10.7 during the current solar cycle while Kumar (2020) had emphasized on how such difference could reduce the performance of IRI-2016.

5. Conclusion

The capability of the IRI-2016 model in reproducing the hemispheric asymmetry, winter and semiannual anomalies has been assessed over Africa. The data were obtained from a chain of GNSS receivers within 25^{o}- 40° E during quiet period of the years 2013 and 2014. We equally analyzed meridional neutral wind and O/N2 ratio measurements in both hemispheres. The results showed that:

(i) The hemispheric asymmetry of the anomaly was clearly depicted by IRI-2016 with the model predicting farther crests location with respect to the magnetic equator in all seasons.

(ii) IRI-2016 overestimated (underestimated) the magnitude of the crests in both hemispheres in December solstice of 2013 (2014) while in June solstice it overestimated it during both years.

(iii) The model predicted the winter anomaly in December solstice but failed to do so in June solstice. It also clearly represented the semiannual anomaly with stronger crests in the northern hemisphere.

(iv) The IRI model reproduced the seasonal trend of variation of the asymmetry index (A) in December solstice and equinox (in the noon). In June solstice, the predicted variation of A was the opposite of what was observed with GNSS-TEC. In addition, the model underestimated (overestimated) the magnitude of A during solstices (equinox) in the noon. In the post sunset, it showed a better agreement with the observed magnitude of A during all seasons except June solstice.

(v) The IRI model misrepresented the hmF2 in both hemispheres during June solstice. This was a likely reason for its inability to predict the winter anomaly. This finding also implied that IRI-2016 failed to capture the variability of the vertical drift and by extension the contribution of meridional wind.

(vi) There was a difference in the seasonal variability of F10.7 and EUV fluxes with the correlation between both parameters varying from 0.27 – 0.90. This implied that F10.7 solar flux which is an input for IRI-2016 did not always capture the changes in EUV flux. F10.7 was thus, a potential source of discrepancies in IRI-2016 in 2013 – 2014.

This is the first study dedicated to assessing the capability of IRI-2016 in reproducing the hemispheric features of the anomaly in Africa during the maximum phase of solar cycle 24. However, it is to be noted that past studies have reported some discrepancies in IRI-2016 over this longitude but with stations located mostly in the northern hemisphere. The present study placed emphasis on the model's performance over both hemispheres using a chain of GNSS receivers and further stressed on the significance of the inclusion of meridional neutral wind and EEJ data for Africa in IRI-2016 in order to improve its performance. The study finally underpinned the contribution

of solar input parameters (e.g., F10.7) as a source of eventual misrepresentation of the observed ionospheric parameters (e.g., TEC).

Acknowledgements

The authors wish to express their appreciation to the following organizations: the UNAVCO (for the GNSS data), the Dominion Radio Astrophysical Observatory (DRAO), Penticton, B.C. (for the solar flux data) and the Space Sciences Center of the University of Southern California (for the SOHO/SEM EUV data). We are also grateful to the IRI development community and GSFC, NASA for the online version of the IRI-2016 model and to IZMIRAN for making available the IRI-Plas model at http://ftp.izmiran.ru/pub/izmiran/SPIM/. Special thanks to the PI (A.B. Christensen) and Project Scientist (L. Paxton) of the GUVI team which provides the O/N_2 data. The wind data were derived from the pyglow package, which is an open-source software available at https://github.com/timduly4/pyglow/.

References

Akala, A. O., Somoye, E.O., Adewale, A.O., Ojutalayo, E.W., Karia, S.P., Idolor, R.O., Okoh, D., Doherty, P.H., 2015. Comparison of GPS-TEC observations over Addis Ababa with IRI-2012 model predictions during 2010–2013, Advances in Space Research, 56, 1686–1698

Amaechi, P. O., Oyeyemi, E. O., Akala, A. O., Falayi, E. O., Kaab, M., Benkhaldoun, Z., et al., 2020. Quiet time ionopheric irregularities over the African Equatorial Ionization Anomaly Region. Radio Science, 55, e2020RS007077. https://doi.org/10.1029/2020RS0077.

Amaechi, P. O., Oyeyemi, E. O., Akala, A. O., 2018. Variability of the African equatorial ionization anomaly (EIA) crests during the year 2013. Canadian Journal of Physics, 97(2), 155–165.

Appleton, E. V., 1946. Two anomalies in the ionosphere. Nature, 157, 691

Appleton, E. V., 1938. Radio transmission and solar activity. Nature, 3594, 142, 499-501.

Balan, N., Bailey, G. J., 1995. Equatorial plasma fountain and its effects: Possibility of an additional layer. Journal of Geophysical Research: Space Physics, 100(A11), 21421-21432.

Berkner, L. V., Wells, H. W., Seaton, S. L., 1936. Characteristics of the upper region of the ionosphere. Terr. Magn. Atmos. Electr., 41(2), 173–184.

Bilitza, D., Altadill, D., Truhlik, V., Shubin, V., Galkin, I., Reinisch, B., Huang, X., 2017. International Reference Ionosphere 2016: from ionospheric climate to real-time weather predictions. Space Weather. 15 (2), 418–429.

Bilitza, D., Reinisch, B. W., 2008. International Reference Ionosphere 2007: Improvement and new parameters, Adv. Space Res., 42, 599–609.

Blewitt, G., 1990. An automatic editing algorithm for GPS data. Geophysical Research Letters, 17(3), 199–202. https://doi.org/10.1029/GL017i003p00199

Burns, A. G., Wang, W., Qian, L., Solomon, S. C., Zhang, Y., Paxton, L. J., Yue, X., 2014. On the solar cycle variation of the winter anomaly, J. Geophys. Res. Space Physics, 119, 4938–4949, doi:10.1002/2013JA019552.

Chartier, A. T., Makela, J. J., Liu, H., Bust, G. S., Noto, J., 2015. Modeled and observed equatorial thermospheric winds and temperatures. Journal of Geophysical Research: Space Physics, 120, 5832–5844. https://doi.org/10.1002/2014JA020921

Cherniak I.V., Zakharenkova, I.E.A. Krankowski , Shagimuratova, I.I., 2012. Plasmaspheric Electron content derived from GPS TEC and FORMOSAT-3/COSMIC measurements: Solar minimum condition. Advances in Space Research 50, 427–440.

Doumouya, V., Cohen, Y., 2004. Improving and testing the empirical equatorial electrojet model with CHAMP satellite data, Ann. Geophys., 22, 3323–3333.

Drob, D. P., Emmert, J. T., Meriwether, J. W., Makela, J. J., Doornbos, E., Conde, M., ... Klenzing, J. H. (2015). An update to the Horizontal Wind Model (HWM): The quiet time thermosphere. Earth and Space Science, 2(7), 301-319.

Emmert, J., Lean, J., Picone, J., 2010. Record-low thermospheric density during the 2008 solar minimum. Geophys. Res. Lett. 37, L12102. https://doi.org/10.1029/2010GL043671.

Endeshaw, L., 2020. Testing and validating IRI-2016 model over Ethiopian ionosphere. Astro-physics and Space Science, 365(3), 1-13.

Estey, L. H., Meertens, C. M., 1999. TEQC: The multi-purpose toolkit for GPS/GLONASS data. GPS Solutions, 3(1), 42–49.

Fejer, B. G., Jensen, J. W., Su, S. Y., 2008. Quiet time equatorial F region vertical plasma drift model derived from ROCSAT-1 observations.Journal of Geophysical Research, 113, A05304. https://doi.org/10.1029/2007JA012801

Fejer, B.G., de Paula, E.R., Heelis, R.A., Hanson, W. B., 1995. Global equatorial ionospheric vertical plasma drifts measured by the AE-E satellite. J. Geophys. Res., 100(A4), 5769– 5776.

Gowtam, V. S., Tulasi Ram, S., 2017. Ionospheric winter anomaly and annual anomaly observed from Formosat-3/COSMIC Radio Occultation observations during the ascending phase of solar cycle 24. Advances in Space Research, 60(8), 1585-1593.

Hansen, A., Blanch, J., Walter, T., 2000. Ionospheric correction analysis for WAAS quiet and stormy (pp. 634–642). ION GPS, Salt Lake City, Utah, September 19–22.

Hargreaves, J. K., 1995. The Solar-Terrestrial Environment: An Introduction to Geospace -The Science of the Terrestrial Upper Atmosphere, Ionosphere, and Magnetosphere, Cambridge Atmos. Space Sci. Ser., vol. 5, Cambridge Univ. Press., New York

Heelis, R. A., Hanson, W. B., 1980. Interhemispheric transport induced by neutral zonal winds in the F region. Journal of Geophysical Research: Space Physics, 85(A6), 3045-3047.

Kaab, M., Benkhaldoun, Z., Fisher, D. J., Harding, B., Bounhir, A., Makela, J. J., et al., 2017. Climatology of thermospheric neutral winds over Oukaïmeden Observatory in Morocco. Annales Geophysicae, 35(1), 161–170. ttps://doi.org/10.5194/angeo-35-161-2017

Karia, S.P., Patel, N.C., Pathak, K.N., 2018. On the performance of IRI-2016 to predict the North-South Asymmetry of the Equatorial Ionization Anomaly around 73°E longitude. Advances in Space Research, 63(6), 1937-1948. https://doi.org/10.1016/j.asr.2018.09.033

Karia, S.P., Patel, N.C., Pathak, K.N., 2015. Comparison of GPS based TEC measurements with the IRI-2012 model for the period of low to moderate solar activity (2009–2012) at the crest of equatorial anomaly in the Indian region. Adv. Space Res. 55 (8), 1965–1975.

Khadka, S. M., Valladares, C. E., Sheehan, R., Gerrard, A. J., 2018. Effects of electric field and neutral wind on the asymmetry of equatorial ionization anomaly. Radio Science, 53(5), 683-697.

Kumar, S., 2020. North-South asymmetry of equatorial ionospheric anomaly computed from the IRI model. Ann. Geophys., 63, 3, doi:10.4401/ag-8324

Kumar, S., 2016. Performance of IRI-2016 model during a deep solar minimum and a maximum year over global equatorial regions. J. Geophys. Res. Space Physics, 121, 5664-5674.

Kwak, Y. S., Kil, H., Lee, W. K., Yang, T. Y., 2019. Variation of the Hemispheric Asymmetry of the Equatorial Ionization Anomaly with Solar Cycle. Journal of Astronomy and Space Sciences, 36(3), 159-168.

Link, R., Cogger, L., 1988. A reexamination of the OI 6300-Å nightglow. J. Geophys. Res., 93(A9), 9883–9892. https://doi.org/10.1029/JA093iA09p09883

Mannucci, A. J., Wilson, B. D., Edwards, C. D., 1993. A new method for monitoring the Earth's ionosphere total electron content using the GPS global network. Proceedings of ION GPS-93, Institute of Navigation (pp. 1323–1332).

Melaku, M., Tsidu, G. M., 2019. Comparison of quite time ionospheric total electron content from IRI-2016 model and GPS observations. Annales Geophysicae https://doi. org/10.5194/angeo-2019-44.

Mengistu T. G., Melaku, Z. M., 2020. Comparison of quiet-time ionospheric total electron content from the IRI-2016 model and from gridded and station-level GPS observations. Annales Geophysicae, 38(3), 725-748.

Mengistu, E., Moldwin, M. B., Damtie, B., Nigussie, M., 2019. The performance of IRI-2016 in the African sector of equatorial ionosphere for different geomagnetic conditions and time scales. Journal of Atmospheric and Solar-Terrestrial Physics, 186, 116-138.

Mengistu, E., Damtie, B., Moldwin, M.B., Nigussie, M., 2018. Comparison of GPS-TEC measurements with NeQuick2 and IRI model predictions in the low latitude East African region during varying solar activity period (1998 and 2008–2015). Advances in Space Research, 61, 1456–1475.

Millward, G. H., Rishbeth, H., Fuller-Rowell, T. J., Aylward, A. D., Quegan, S., Moffett, R. J., 1996. Ionospheric F2 layer seasonal and semiannual variations, J. Geophys. Res., 101(A3), 5149–5156.

Mitra, S.K., 1946. Geomagnetic control region F2 of the ionosphere. Nature 158, 668-669.

Namba, S., Maeda, K.-I., 1939. Radio Wave Propagation, 86 pp., Corona, Tokyo

Oyedokun, O. J., Akala, A. O., Oyeyemi, E. O., 2020. Characterization of African Equatorial Ionization Anomaly (EIA) during the maximum phase of solar cycle 24. Journal of Geophysical Research: Space Physics. doi:10.1029/2019ja027066.

Paul, A., DasGupta, A., 2010. Characteristics of the equatorial ionization anomaly in relation to the day-to-day variability of ionospheric irregularities around the post sunset period. Radio Science, 45, RS6001.

Qian, L., Burns, A. G., Wang, W., Solomon, S. C., Zhang, Y., Hsu, V., 2016. Effects of the equatorial ionosphere anomaly on the interhemispheric circulation in the thermosphere, J. Geophys. Res. Space Physics, 121, doi:10.1002/2015JA022169.

Qian, L., Yue, J., 2017. Impact of the lower thermospheric winter-to-summer residual circulation on thermospheric composition, Geophys. Res. Lett., 44, 3971–3979, doi:10.1002/2017GL073361.

Rishbeth, H., Muller-Wodarg, I. C. F., Zou, L., Fuller-Rowell, T. J., Millward, G. H., Moffett, R. J., Idenden, D. W., Aylward, A. D., 2000. Annual and semiannual variations in the ionospheric F2-layer: II. Physical discussion, Ann. Geophys., 18, 945–956. http://www.ann-geophys.net/18/945/2000/

Rishbeth H. 1998. How the thermospheric circulation affects the ionosphere. J. Atm Sol-Terr Phys 60: 1385–1402. DOI: 10.1016/S1364-6826(98)00062-5.

Rishbeth, H., Setty, C.S.G.K., 1961. The F-layer at sunrise. Journal of Atmospheric and Terrestrial Physics, 20(4), 263-276.

Sardon, E., Rius, A., Zarraoa, N., 1994. Estimation of the transmitter and receiver differential biases and the ionospheric total electron content from GPS observations. Radio Science, 29(3), 577–586. https://doi.org/10.1029/94RS00449

Scherliess, L., Fejer, B. G., 1999. Radar and satellite global equatorial F region vertical drift model. J Geophys Res 104(A4): 6829–6842.

Seemala, G., Delay, S. B., 2010. GNSS TEC data processing. 2nd Workshop on Satellite

Navigation Science and Technology for Africa, Trieste, 6–24 April 2010.

Silva, A. L. A., Sousasantos, J., Marini-Pereira, L., Lourenço, L. F. D., Moraes, A. O., Abdu, M. A., 2020. Evaluation of the dusk and early nighttime Total Electron Content modeling over the eastern Brazilian region during a solar maximum period. Advances in Space Research. doi.org/10.1016/j.asr.2020.12.015

Sousasantos, J., Abdu, M. A., Santos, A., Batista, I., Silva, A., Lourdes, L. E., 2020. Further complexities on the pre-reversal vertical drift modeling over the Brazilian region: A comparison between long-term observations and model results. J. Space Weather Space Clim. 10, 20. ttps://doi.org/10.1051/swsc/2020022

Sterling, D. L., Hanson, W. B., Moffett, R. J., Baxter, R. G., 1969. Influence of electromagnetic drifts and neutral air winds on some features of the F 2 region. Radio Sci.4, 1005–1023.

Tariku, Y. A., 2020. Comparison of performance of the IRI 2016, IRI Plas 2017, and NeQuick 2 models during different solar activity (2013–2018) years over South American sector. Radio Science, 55(8), 1-17.

Titheridge, J. E., 1995. Winds in the ionosphere - A review. Journal of Atmospheric and Terrestrial Physics, 57(14), 1681-1714.

Torr, M.R., Torr, D.G., 1973. The seasonal behaviour of the F2-layer of the ionosphere. J Atm. Terr. Phys., 35: 2237–2251. DOI:10.1016/0021- 9169(73)90140-2.

Tulasi Ram, S., Su, S. Y., Liu, C. H., 2009. FORMOSAT-3/COSMIC observations of seasonal and longitudinal variations of equatorial ionization anomaly and its interhemispheric asymmetry during the solar minimum period. Journal of Geophysical Research: Space Physics, 114(A6).

Yasyukevich, Y.V., Yasyukevich, A.S., Ratovsky, K.G., Klimenko, M.V., Klimenko, V. V., Chirik, N.V., 2018. Winter anomaly in NmF2 and TEC: when and where it can occur. Journal of Space Weather and Space Climate, 8, A45.

Venkatesh, K., Fagundes, P. R., Prasad, D. S. V. V. D., Denardini, C. M., de Abreu, A.J., de Jesus, R., Gende, M., 2015. Day-today variability of equatorial electrojet and its role on the day-to-day characteristics of the equatorial ionization anomaly over the Indian and Brazilian sectors, J. Geophys. Res. Space Physics, 120, doi:10.1002/2015JA021307.

Yonezawa, T., Arima, Y., 1959. On the seasonal and non-seasonal annual variations and

the semi-annual variation in the noon and midnight electron densities of the F2 layer in middle latitudes. J. Radio Res. Labs., 6, 293– 309.

Zhao, B., Wan, W., Liu, L., Mao, T., Ren, Z., Wang, M., Christensen, A. B., 2007. Features of annual and semiannual variations derived from the global ionospheric maps of total electron content. Ann. Geophys., 25, 2513–2527

Zeng, Z., Burns, A. G., Wang, W., Lei, J., Solomon, S.C., Syndergaard, S., Qian, L., Kuo, Y.-H., 2008. Ionospheric annual asymmetry observed by the COSMIC radio occultation measurements and simulated by the TIEGCM. J. Geophys. Res., 113, A07305, doi:10.1029/2007JA012897

Zou, L., Rishbeth, H., Müller-Wodarg, I.C.F., Aylward, A.D., Millward, G.H., Fuller-Rowell, T.J., Idenden, D.W., Moffett, R.J., 2000. Annual and semiannual variations in the ionospheric F2-layer. I. Modelling. Ann Geophys 18: 927–944. DOI: 10.1007/s00585-000-0927-8.

Table Caption

Table 1 : data sets

Figure Captions

Fig. 1. Geogaphic locations of the GNSS stations used: the magenta solid curve indicates the magnetic equator (dip = 0) while the horizontal green curves indicate ±20 degree dip latitudes.

Fig. 2. Seasonal variations of the EIA reconstructed using GNSS -TEC and IRI-TEC during solstices of years 2013 - 2014. The horizontal black lines represent the magnetic equator.

Fig. 3. Noon and post sunset variations of the: (a-b) asymmetry index (A) in solstices of years 2013 -2014 and (c-d) maximum height of the F2 layer (hmF2) in year 2013. A was computed with TEC derived from GNSS and predicted by IRI, respectively.

Fig. 4. Variations of GNSS-TEC and IRI-TEC in equinox and solstices in the years 2013 and 2014. The horizontal black lines represent the magnetic equator.

Fig. 5. Changes in the asymmetry index during equinox and solstices of 2013 and 2014.

Fig. 6. Seasonal variations in O/N_2 ratio in both hemispheres from 2013 to 2014.

Fig. 7. Seasonal variations of thermospheric neutral wind velocity in the years 2013 and 2014. The broken horizontal lines represent the magnetic equator.

Fig. 8. Seasonal correlation between EUV flux (26–34 nm) and F10.7 solar flux in year 2013 and 2014.

Table 1

S/N	Data	Organization /Instrument	Data link
1	GNSS-TEC	UNAVCO	www.unavco.com
2	IRI-TEC	COSPAR/URSI	https://ccmc.gsfc.nasa.gov/modelweb/models/iri2016_vitmo.php
3	O/N_2 ratio	GUVI	guvitimed.jhuapl.edu
4	EUV	SEM/SOHO	https://soho.nascom.nasa.gov/data/data.html
5	F10.7	DRAO	http://www.spaceweather.gc.ca/solarflux/sx-5-en.php
6	Kp	ISGI	isgi.unistra.fr

UNAVCO- University Navstar Consortium
SEM - Solar EUV Monitor;
SOHO - Solar Heliophysical Observatory (SOHO)
DRAO-Dominion Radio Astrophysical Observatory
ISGI- International Service of Geomagnetic Indices

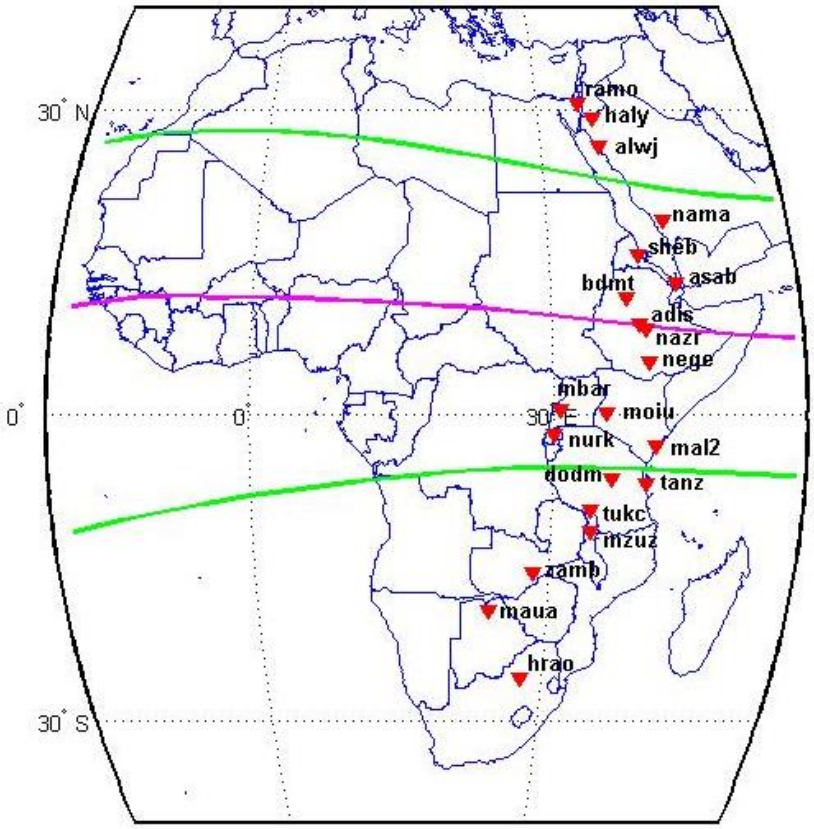

Fig. 1. Geogaphic locations of the GNSS stations used: the magenta solid curve indicates the magnetic equator (dip = 0) while the horizontal green curves indicate ±20 degree dip latitudes.

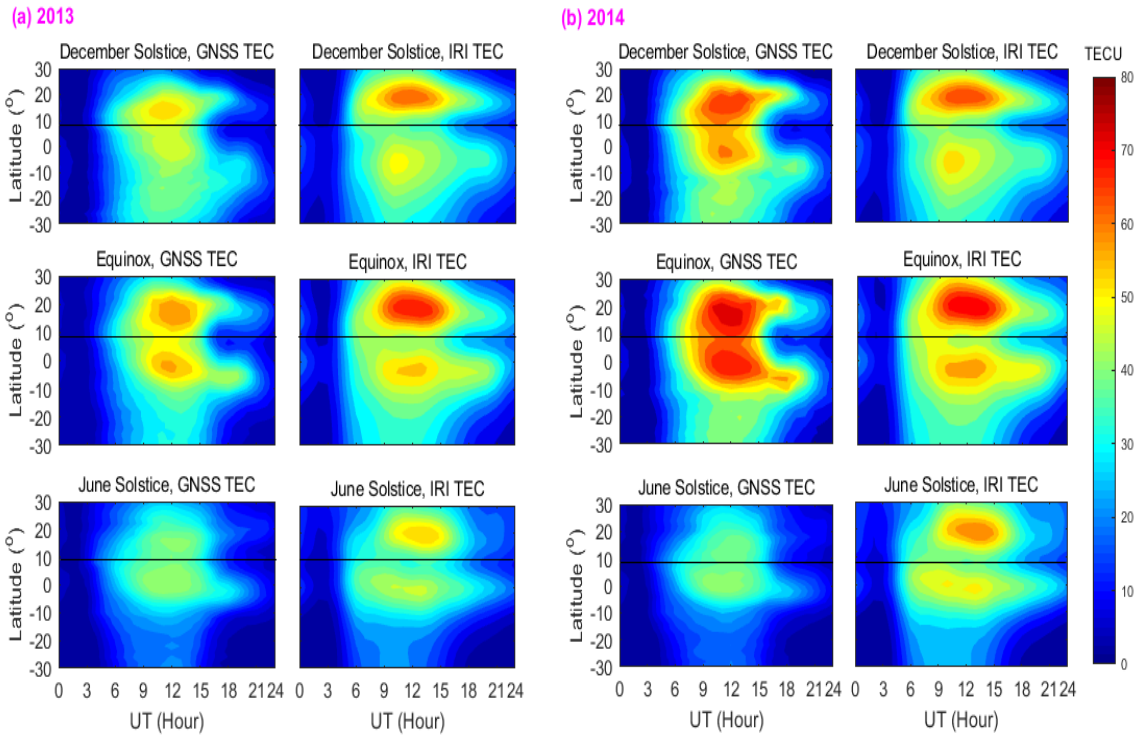

Fig. 2. Seasonal variations of the EIA reconstructed using GNSS -TEC and IRI-TEC during solstices of years 2013 - 2014. The horizontal black lines represent the magnetic equator.

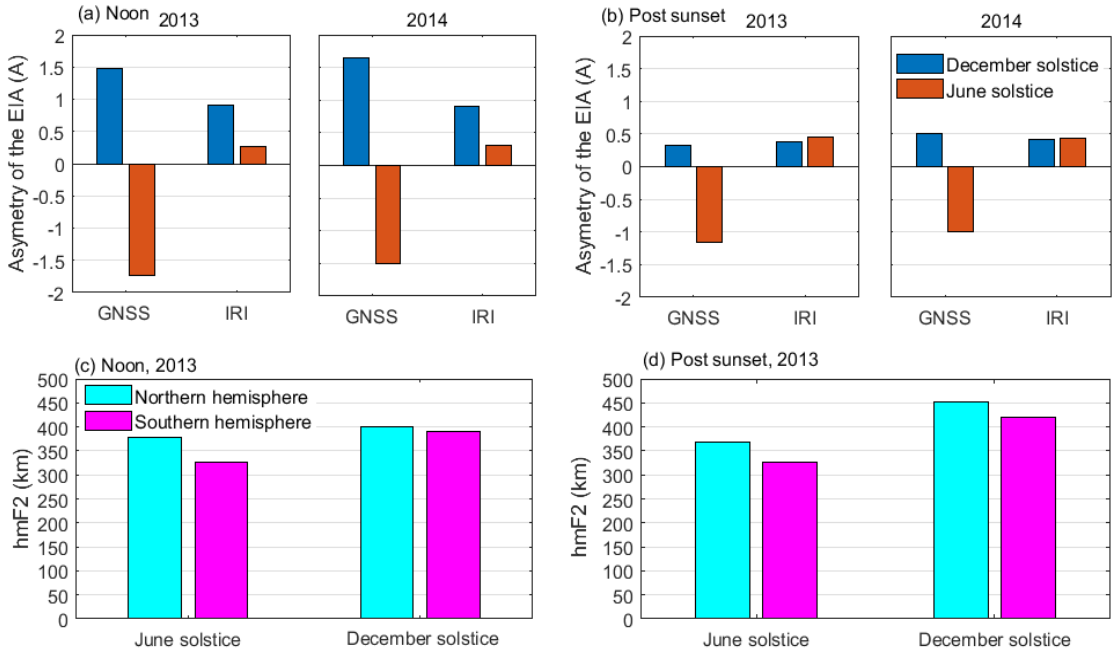

Fig. 3. Noon and post sunset variations of the: (a-b) asymmetry index (A) in solstices of years 2013 -2014 and (c-d) maximum height of the F2 layer (hmF2) in year 2013. A was computed with TEC derived from GNSS and predicted by IRI, respectively.

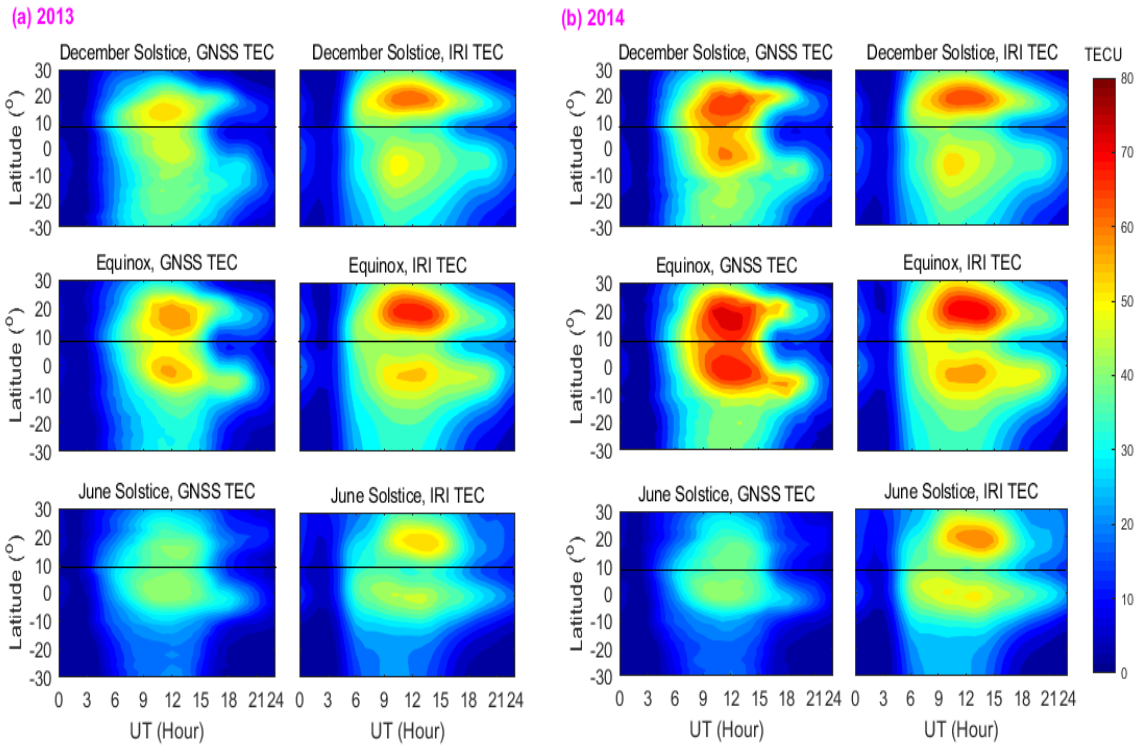

Fig. 4. Variations of GNSS-TEC and IRI-TEC in equinox and solstices in the years 2013 and 2014. The horizontal black lines represent the magnetic equator.

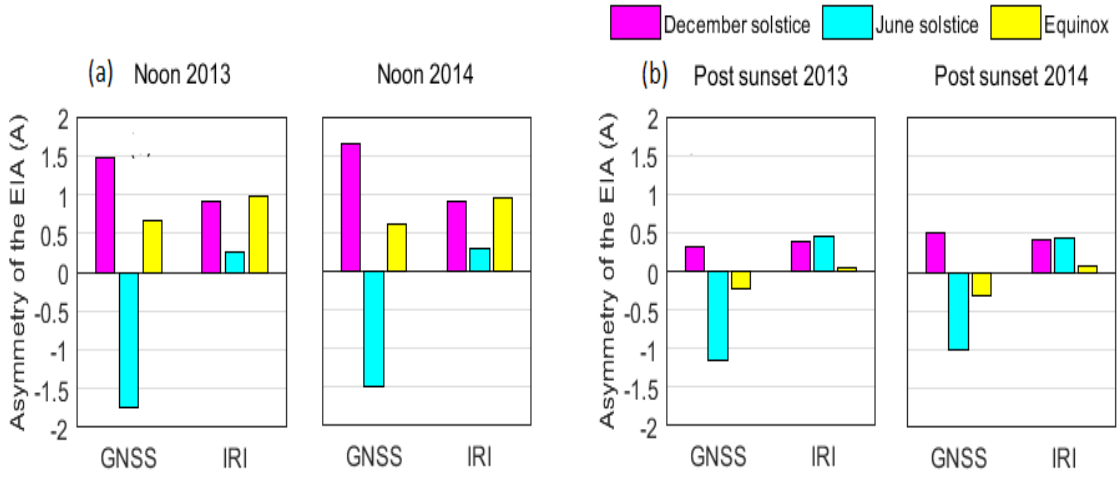

Fig. 5. Changes in the asymmetry index during equinox and solstices of 2013 and 2014.

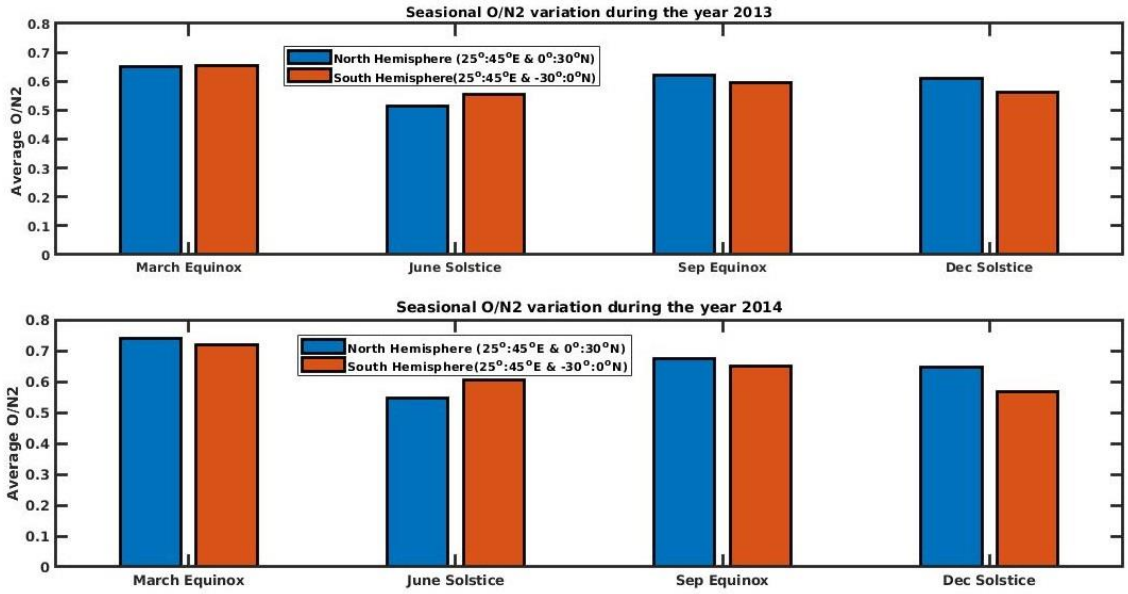

Fig. 6. Seasonal variations in O/N_2 ratio in both hemispheres from 2013 to 2014.

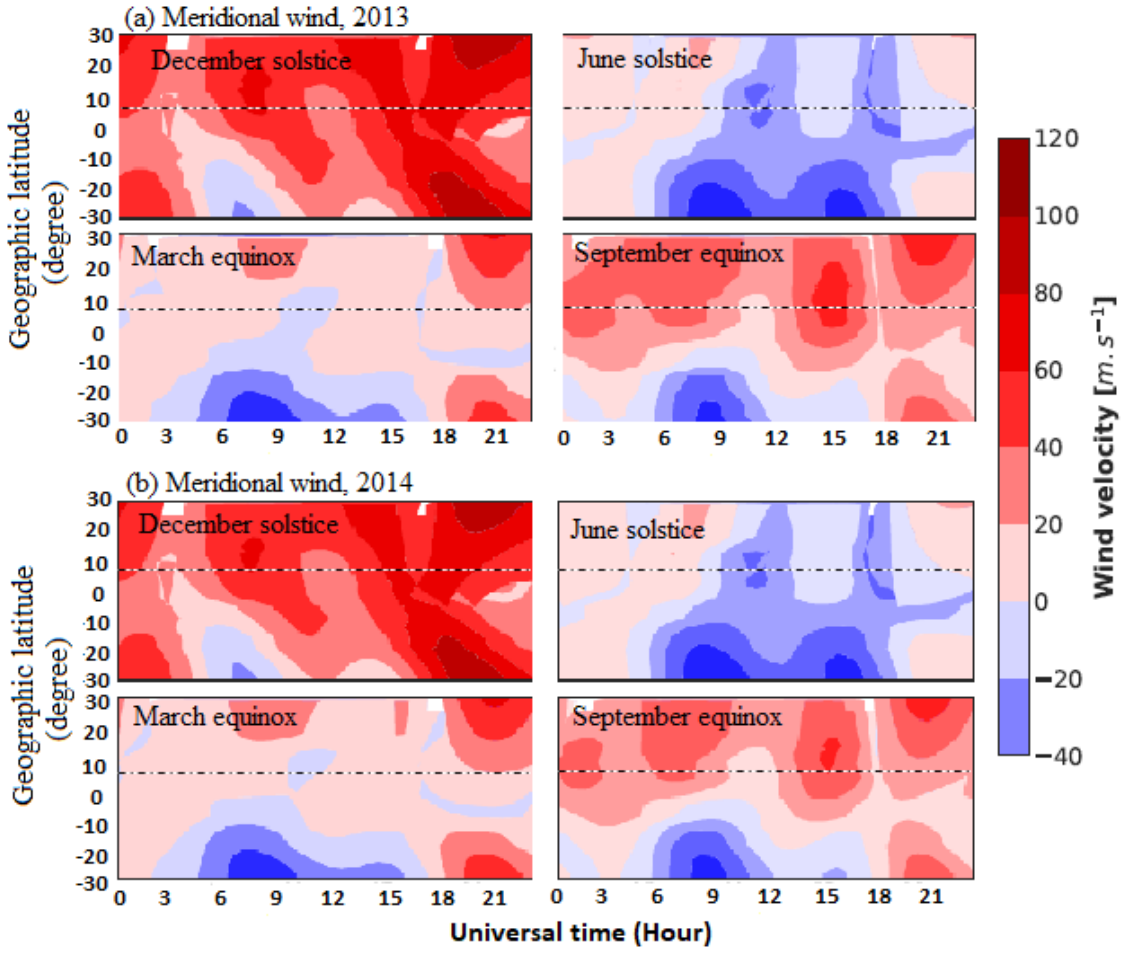

Fig. 7. Seasonal variations of thermospheric neutral wind velocity in the years 2013 and 2014. The broken horizontal lines represent the magnetic equator.

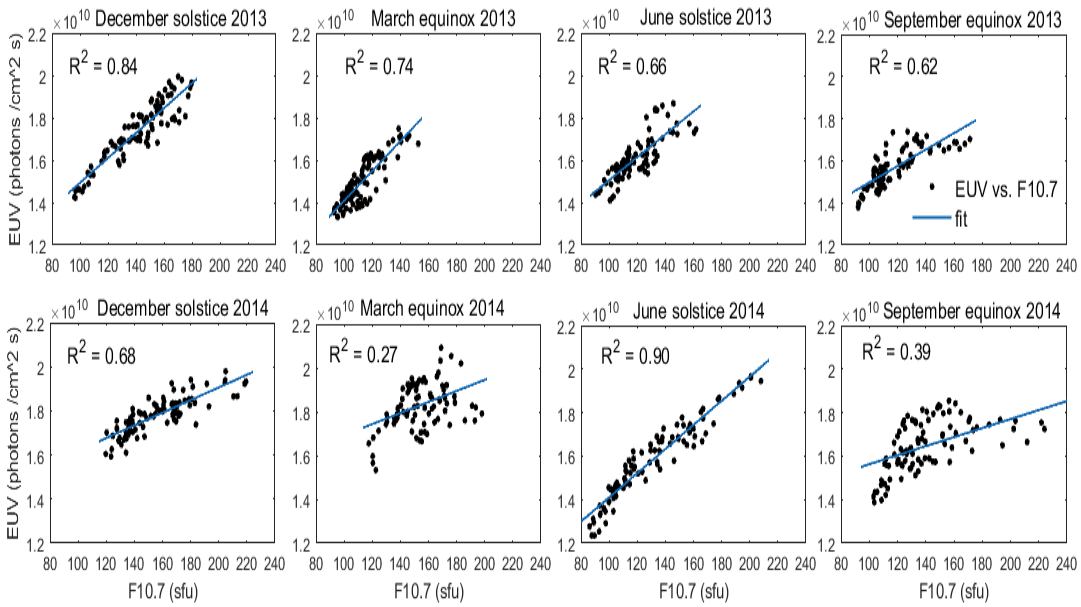

Fig. 8. Seasonal correlation between EUV flux (26–34 nm) and F10.7 solar flux in year 2013 and 2014.